Solar extreme-ultraviolet irradiance for general circulation models

Stanley C. Solomon and Liying Qian
High Altitude Observatory, National Center for Atmospheric Research, Boulder, Colorado, USA

Received 31 March 2005; revised 30 June 2005; accepted 12 July 2005; published 20 October 2005.

[1] Recent measurements of the solar extreme-ultraviolet spectrum provide high-resolution spectral irradiance that can be used for calculating ionization and dissociation rates in the upper atmosphere and for providing improved proxy-based models of the solar spectrum. These are crucial inputs for global time-dependent general circulation models of the thermosphere and ionosphere, but computational economies require that a lower-resolution spectrum be used in the calculations without excessive loss of accuracy. The problem is compounded by the photoelectrons generated by ionization, which cause further ionization and dissociation of atmospheric gases. We describe a method for using solar spectral measurements or models to calculate ionization and dissociation rates throughout the upper atmosphere, including photoelectron effects, that is more accurate and more efficient than its predecessors. Examples of use with measurements from the Solar EUV Experiment on the TIMED satellite and with the EUVAC model are given, and an example calculation using the National Center for Atmospheric Research thermosphere-ionosphere-electrodynamics general circulation model is shown.

Citation: Solomon, S. C., and L. Qian (2005), Solar extreme-ultraviolet irradiance for general circulation models, *J. Geophys. Res.*, *110*, A10306, doi:10.1029/2005JA011160.

1. Introduction

[2] Solar extreme ultraviolet radiation and soft X rays shortward of 105 nm are absorbed by the terrestrial thermosphere above ~90 km, primarily by ionization of the major species N_2, O, and O_2. This process creates the ionosphere and also leads to dissociation of the molecular species through direct photodissociation and many indirect processes driven by ionization. The most important of these indirect processes is the generation of energetic electrons which carry the excess energy transferred by photoionization. These photoelectrons can further ionize, dissociate, and excite neutral constituents, and the products initiate a sequence of elastic and inelastic processes that channel the initial photon energy into kinetic energy of the thermosphere and ionosphere. The extreme ultraviolet (EUV) and X-ray region is the most variable part of the solar spectrum, with the solar cycle variation ranging from about a factor of two through most of the EUV to more than an order of magnitude in parts of the X-ray spectrum, and additional rotational, daily, and short-term variability.

[3] Measurements and models of solar EUV and X-ray irradiance have been recently reviewed by *Woods et al.* [2004]. Early measurements in the extreme ultraviolet (EUV) region from the SOLRAD, AEROS, and OSO satellites, and rocket experiments by the Air Force Cambridge Research Laboratories, led to comprehensive measurements by instruments on the Atmosphere Explorer satellites and associated calibration rocket flights [e.g., *Hall et al.*, 1969; *Hall and Hinteregger*, 1970; *Reeves and Parkinson*, 1970; *Schmidtke et al.*, 1977; *Heroux and Higgins*, 1977; *Hinteregger et al.*, 1981]. These data form the basis for many of the reference spectra and empirical models used in thermosphere/ionosphere research over the intervening years [e.g., *Donnelly*, 1976; *Hinteregger et al.*, 1981; *Richards et al.*, 1994; *Tobiska et al.*, 2000; *Woods and Rottman*, 2002]. During the 1990s, most of the available measurements were broadband rather than spectrally resolved [e.g., *Feng et al.*, 1989; *Ogawa et al.*, 1990; *Judge et al.*, 1998; *Acton et al.*, 1999; *Bailey et al.*, 1999a, 1999b, 2000, 2001] with the exception of short-term measurements from the San Marcos satellite [*Schmidtke et al.*, 1992] and rocket flights [*Woods et al.*, 1998a]. Another important development during this period was the advent of semi-theoretical models based on an observational emission measure approach [*Warren et al.*, 2001].

[4] Despite this history, significant uncertainties in the magnitude and variation of this region of the solar spectrum remain. This is particularly the case for the soft X-ray to hard EUV region of the solar spectrum from 1 to ~30 nm, sometimes designated "XUV," but there are still significant questions concerning important EUV features such as the He II 30.4 nm, C III 97.7 nm, and H Lyman-β 102.6 nm lines. With launch of the Thermosphere-Ionosphere-Mesosphere Energetics and Dynamics (TIMED) satellite in December 2001, we have new, high-quality measurements spanning solar maximum to near-minimum conditions from the Solar EUV Experiment (SEE) [*Woods et al.*, 1998b, 2005]. SEE consists of two instruments, an EUV grating spectrograph (EGS) that measures the range 27–180 nm at 0.4 nm resolution and an X-ray photodiode system (XPS) that observes the 0.1–30 nm range using broadband photodiode measurements with spectral resolu-

0148-0227/05/2005JA011160$09.00

tion on the order of ~5 to ~10 nm. These measurements are now supplemented by a similar XPS instrument on the SORCE spacecraft, launched in January 2003. These observations should resolve most of the outstanding questions, but because the XPS is a broadband instrument and because the solar spectrum is still not well-known in the soft X-ray region, disagreements over the effective calibration and interpretation of the photodiode measurements remain.

[5] The SC21REFW reference spectrum and scaling factors obtained from the Atmosphere Explorer (AE) program and associated rocket measurements by *Hinteregger et al.* [1981] (HFG) has been thought to underestimate the irradiance shortward of ~25 nm. The problem dates back to comparisons with AE photoelectron measurements by *Richards and Torr* [1984] and is reviewed by *Solomon* [1991] and *Bailey et al.* [2000]. The EUVAC model of *Richards et al.* [1994], largely based on an earlier AE reference spectrum (F74113), increases the fluxes below 25 nm by factors of 2 to 3, based on a reanalysis of the solar data and on photoelectron spectra. Broadband measurements from rockets [e.g., *Feng et al.*, 1989; *Ogawa et al.*, 1990; *Bailey et al.*, 1999a] and from the SNOE satellite [*Solomon et al.*, 1996; *Bailey et al.*, 1996, 2000, 2001] support this, as does subsequent analysis of ion density and photoelectron fluxes [*Winningham et al.*, 1989; *Buonsanto et al.*, 1992, 1995; *Solomon et al.*, 2001]. The SEE XPS measurements also support an increase in the HFG spectrum in the XUV but are lower in magnitude than contemporaneous SNOE observations and slightly lower than EUVAC in an integral sense [*Solomon*, 2005]. The *Warren et al.* [2001] model yields lower values than either of these observations in the 5–25 nm range, although still greater than HFG, and recently *Strickland et al.* [2004], in an analysis based on ultraviolet airglow emissions, advocate little or no increase from the HFG model values.

[6] Given these uncertainties, why concern ourselves with the accurate application of solar spectral irradiance to numerical models of the thermosphere/ionosphere? For the EUV range, the uncertainties are greatly reduced by the new data and models; for soft X rays, it is equally important to fully account for the energy deposition process as it is to get the spectral magnitude correct. Historically, numerical models have underestimated total ionization and odd nitrogen production in the lower thermosphere (the ionospheric *E* region), due to a variety of reasons, including neglect of photons shortward of 5 nm and underestimation of photoelectron effects as well as inadequate irradiance levels. These two problems largely motivate the present work.

[7] Specification of the solar EUV irradiance is necessary for calculation of thermospheric temperature and ionospheric density, either in an indexed fashion as may be employed by empirical models or as an explicit formulation for numerical models. For detailed process models, commonly with a single spatial dimension (altitude), a high-resolution spectrum at 0.1 nm or 1.0 nm may be employed, but for time-dependent global general circulation models the spectrum is generally divided into coarser resolution segments because the calculation of altitude-dependent ionization rates for each spectral interval, each atmospheric species, each model grid point, and each time step becomes a large fraction of total computational effort. Furthermore, the additional ionization and dissociation that occurs as a consequence of the energetic electrons generated by ionization must be accounted for in some parametric fashion. The purpose of this work is to introduce an improved method that handles EUV processes for large-scale numerical models in a manner that is more accurate and more efficient than past methods.

2. Construction of the Low-Resolution Spectrum

2.1. Solar EUV Spectrum

[8] The goals of a new low-resolution solar spectrum structure for general circulation models are to increase model accuracy by obtaining improved agreement with high-resolution calculations and to increase computational efficiency by reducing the number of spectral intervals. The basic principles in addressing this problem are that the atmosphere responds to solar irradiance, depending upon the cross sections of major species and their relative densities and on the amount of energy transmitted by the various regions of the spectrum. The scheme described here does not divide the spectrum into uniform segments or isolate bright lines but rather uses coarse resolution where the cross sections change slowly with wavelength and high resolution where the cross sections have complex structure. The basic criteria for the interval boundaries are that the change in cross section within each bin should be minimized, and the change in photon energy of should be less than a factor of ~2. Also, variable structure in the solar spectrum must be considered. To illustrate the problem, Figure 1a displays the SC21REFW and F79050 high-resolution standard reference spectra [*Hinteregger et al.*, 1981] with the cross sections of major atmospheric species superimposed. Although both have regions of high structure and variation, fortunately the regions where both solar spectrum and atmospheric cross sections are highly structured are relatively small. This is because the ionization continua cross sections shortward of ~70 nm overlap the regions dominated by coronal and chromospheric lines, and the dissociation bands and threshold effects in the 70–91 nm region coincide with the H Lyman continuum. Nevertheless, there are some problem areas, such as where bright hydrogen and carbon lines in the 90–105 nm range interact with band structure and ionization thresholds in N_2 and O_2. Figure 1b shows the result of the interaction of the solar spectrum with thermospheric gases in the form of color contours of local energy deposition as a function of wavelength and altitude. Each interval in the spectral direction (1-nm resolution is employed to make this plot) is essentially a Chapman function with peak altitude determined by the total of the major species cross sections, and the total energy deposition is thus a superposition of many such functions.

[9] The low-resolution spectrum was constructed by applying the basic principles described above and then adjusting the number of bins and their boundaries by trial and error until good agreement between high-resolution and low-resolution calculations was obtained. The resulting structure uses the 22 intervals specified in Table A1 (see Appendix A). Starting at the shortest wavelengths, the first two bins correspond to the two channels of the GOES X-ray sensors, and the third corresponds to the starting point of the *Hinteregger et al.* [1981] reference spectrum. The next

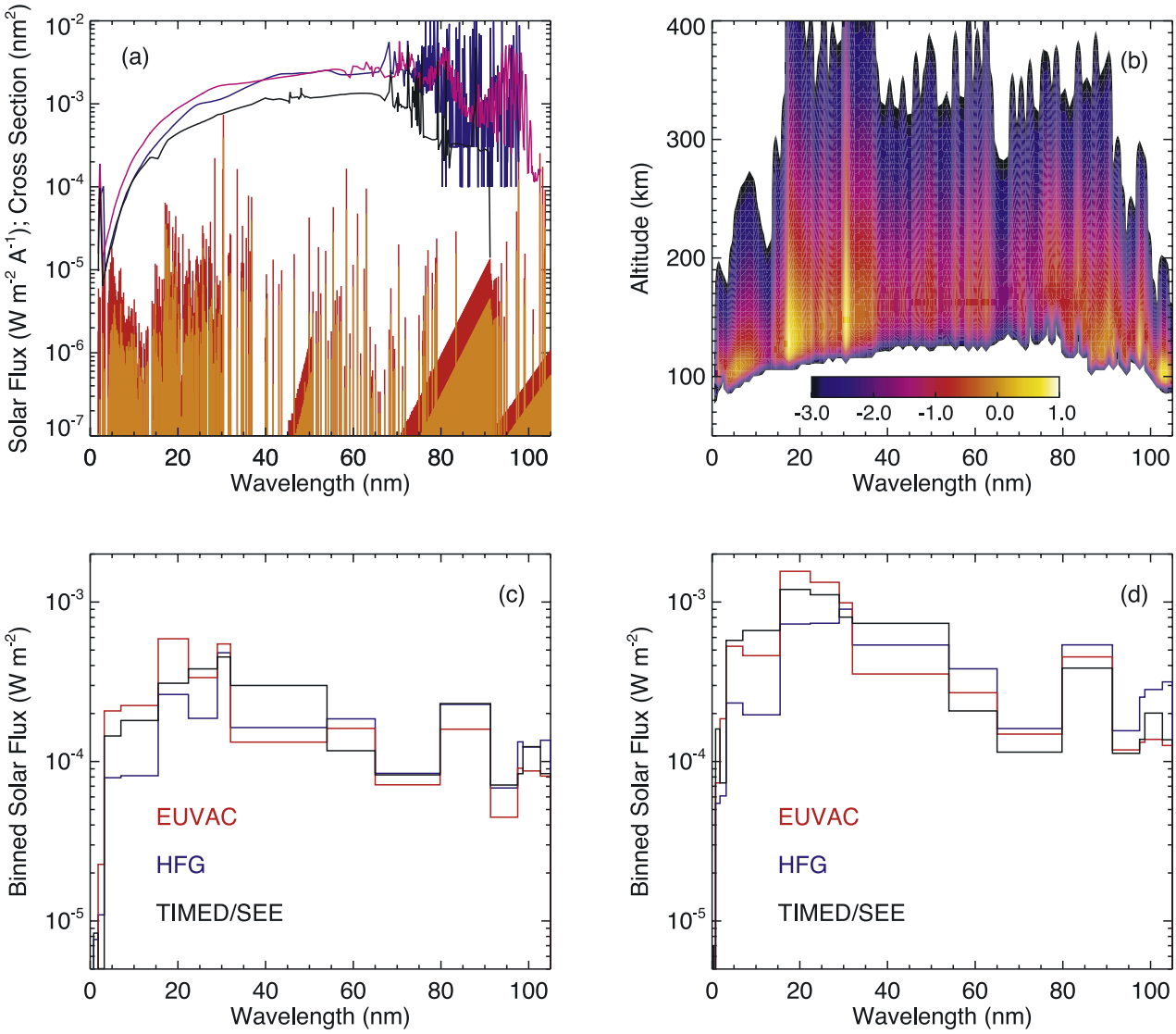

Figure 1. (a) Solar spectral irradiance and atmospheric cross sections. The solar spectra are taken from the SC21REFW (low activity) and F79050 (high activity) reference spectra [*Hinteregger et al.*, 1981]; the cross sections are from *Fennelly and Torr* [1992] and *Henke et al.* [1993]. Orange: low activity solar irradiance; red: high activity solar irradiance; black: atomic oxygen cross section; magenta: O_2 cross section; blue: N_2 cross section. (b) Deposition of solar EUV energy in the thermosphere as a function of wavelength and altitude in $\log_{10}(\mathrm{Wm}^{-4})$ for low solar activity. (c) HFG [*Hinteregger et al.*, 1981] and EUVAC [*Richards et al.*, 1994] proxy models in the new low-resolution bin structure for $F_{10.7} = \langle F_{10.7} \rangle = 80$, and data from the TIMED/SEE instrument [*Woods et al.*, 2005] at moderately low solar activity on 30 March 2004 ($F_{10.7} = 77$, $\langle F_{10.7} \rangle = 84$). Blue: HFG; red: EUVAC; black: SEE. (d) HFG, EUVAC, and data from TIMED/SEE at moderately high solar activity on 8 February 2002 ($F_{10.7} = 186$, $\langle F_{10.7} \rangle = 204$). Blue: HFG; red: EUVAC; black: SEE.

extends to the *k* shell threshold for nitrogen, and subsequent bins through the ionization continua proceed at progressively larger intervals corresponding to the progressively smaller change in cross section magnitude. There is a relatively narrow band at 29–32 nm to enclose the important He II line at 30.4 nm. In the regions where significant band structure occurs, multiple overlapping bins are used, two in the 65.0–79.8 nm range and three in the 79.8–91.3 nm and 91.3–97.5 nm ranges, in order to obtain a broader and more realistic altitude distribution of energy deposition than would be calculated using single bins. The boundaries of these ranges are determined by the ionization thresholds for N_2 and O, respectively. The following narrow bin contains the bright C III line at 97.7 nm, which, because it falls in a region of very low N_2 cross section but is a significant contributor to O_2 ionization, requires independent treatment. The penultimate interval contains H Lyman-β and ends at the O_2 ionization threshold, and the last extends to 105 nm for compatibility with existing standards for the EUV spectral range.

[10] The procedure for calculating irradiance and effective cross sections for the multiple overlapping bins is as

follows. The strategy is to sort the high-resolution spectrum into categories based on the N_2 total absorption cross section. First, the model or measured spectrum in each interval is distributed proportionally onto the SC21REFW spectrum at 0.1 nm resolution. The N_2 cross section in each of these high-resolution intervals is then interpolated from the *Fennelly and Torr* [1992] compilation and the irradiance in each low-resolution bin integrated for high ($\sigma > 3.1 \times 10^{-17}$ cm^2), medium (3.1×10^{-17} cm$^2 > \sigma > 4.0 \times 10^{-18}$ cm^2), and low ($\sigma < 4.0 \times 10^{-18}$ cm^2) categories. (The 65.0–79.8 nm bin uses only the high and medium categories.) The effective cross section for each low-resolution bin is computed as the irradiance-weighted average of the high-resolution cross sections for that category.

[11] The HFG and EUVAC solar proxy models have been adapted to this structure. The HFG model employs a two-class contrast ratio method, with each line or spectral interval characterized as either a chromospheric (class 1) or coronal (class 2) emission. Each line or interval is then scaled by the product of its contrast ratio and the enhancement factor for that class. In Hinteregger's original formulation, the enhancement factor was based on the ratio of H Lyman β (102.6 nm) to its low-activity value for chromospheric emissions and the ratio of Fe XVI (33.5 nm) to its low-activity value for coronal emissions. For periods where these enhancement ratios were not measured, they may be estimated from a relationship based on the $F_{10.7}$ index. The high-resolution spectrum, based on the SC21REFW reference file, has been integrated into the low-resolution intervals and the contrast ratios summed into a scale factor for each class. The spectral intervals, reference values, and contrast ratios, are specified in the first five columns of Table A1 (see Appendix A). To scale the spectrum based on $F_{10.7}$ and its 81-day centered mean $\langle F_{10.7} \rangle$, the following formula is employed:

$$f(\lambda) = f_{\mathrm{ref}}(\lambda) + r_1 c_1(\lambda) + r_2 c_2(\lambda), \quad (1)$$

where f_{ref} is the binned reference spectrum, c_k are the contrast ratios obtained from Table A1, and

$$\begin{aligned} r_1 &= 0.0138(F_{10.7} - 71.5) + 0.005(F_{10.7} - \langle F_{10.7} \rangle + 3.9) \\ r_2 &= 0.5943(F_{10.7} - 71.5) + 0.381(F_{10.7} - \langle F_{10.7} \rangle + 3.9). \end{aligned} \quad (2)$$

The EUVAC model employs a simpler scaling method using the factor $P = (F_{10.7} + \langle F_{10.7} \rangle)/2$ and:

$$f(\lambda) = f_{\mathrm{ref}}(\lambda)[1 + A(\lambda)(P - 80)], \quad (3)$$

where f_{ref} is the binned reference spectrum and A is a scale factor, based on the *Richards et al.* [1994] values. Because the published values are tabulated using the *Torr et al.* [1979] scheme, the low-resolution EUVAC spectrum was calculated by scaling the SC21REFW spectrum to the EUVAC values for each interval and then rebinning them into the new intervals. The reference spectrum and A factors for EUVAC are given in columns 6 and 7 of Table A1.

[12] Between 1.8 and 5 nm, where the *Torr et al.* [1979] spectrum and hence EUVAC do not extend, the HFG model was employed for the EUVAC spectrum, but multiplied by a factor of 3 for consistency with the scale factors used by *Richards et al.* [1994] in the 5–10 nm range. For the range from 0.8 to 1.8 nm, quantitative information on the solar spectrum and its variability is scant. Values were estimated from a variety of sources, including *DeJager* [1964], *Smith and Gottlieb* [1974], *Manson* [1977], *Kreplin et al.* [1977], and *Horan and Kreplin* [1981]. The values given should be considered as very preliminary at this time since the *Warren et al.* [2001] model and hence SEE spectral estimates give significantly larger values in the 0.8–1.8 nm range. For the 0.05 to 0.4 nm and 0.4 to 0.8 nm intervals, a simple linear fit to data from the GOES-8 X-ray sensor during 1995–2003 was employed [c.f., *Wagner*, 1988].

[13] These models, binned into the low-resolution scheme and scaled for low and high solar activity, are shown in Figures 1c and 1d. In Figure 1c, scaled values for $F_{10.7} = \langle F_{10.7} \rangle = 80$ are plotted, and data from TIMED SEE (level 3, version 8) for 30 March 2005. The solar radio flux values were $F_{10.7} = 77$, $\langle F_{10.7} \rangle = 84$, $P = 81$, the lowest activity measured by SEE to date. Figure 1d shows the HFG and EUVAC models compared to data from TIMED/SEE for 8 February 2002 (the day of the initial calibration rocket flight and the first day in the SEE data base). The solar radio flux values were $F_{10.7} = 186$, $\langle F_{10.7} \rangle = 204$, $P = 195$ on this day. Unsurprisingly, there are differences between SEE and both models, but in general the EUVAC model does a reasonable job of describing the SEE measurements. Although there are interval-by-interval differences in the soft X-ray region, the integrated XUV is in fair agreement, and considerably larger than the HFG model. We note that the broadband photodiodes on the XPS channel of SEE perform better as integrated energy detectors than as spectral analyzers. Conversely, at the longer wavelengths, SEE tends to support the lower values at high solar activity predicted by EUVAC.

2.2. Computation of Photoionization and Photodissociation Rates

[14] Several compilations of cross sections of major thermospheric species have been published that are useful for aeronomical calculations, e.g., *Kirby et al.* [1979], *Conway* [1988], and *Fennelly and Torr* [1992]. Each of these represents an update to the last with improvements from more recent measurements, particularly with respect to atomic oxygen revisions, and the Fennelly and Torr compilation has higher resolution in the structured dissociation band region. Therefore the Fennelly and Torr compilation is used as the starting point, but state-specific and dissociative ionization branching ratios are obtained from Conway et al. Shortward of 5 nm, the cross sections calculated by *Henke et al.* [1993] are used.

[15] Cross sections for each major thermospheric gas are calculated for the low-resolution spectrum by averaging the high-resolution cross section spectrum within each interval, weighted by the solar energy flux at each wavelength. The total cross section for each bin is calculated, and then the specific processes are expressed as branching ratios. For O, shown in Table A2, branching ratios for ionization to the $O^+(^4S)$, $O^+(^2D)$, and $O^+(^2P)$ and given. For O_2 and N_2, shown in Tables A3 and A4, branching ratios for ionization, dissociative ionization, and dissociation are specified. Additional state-specific branching ratios can be calculated

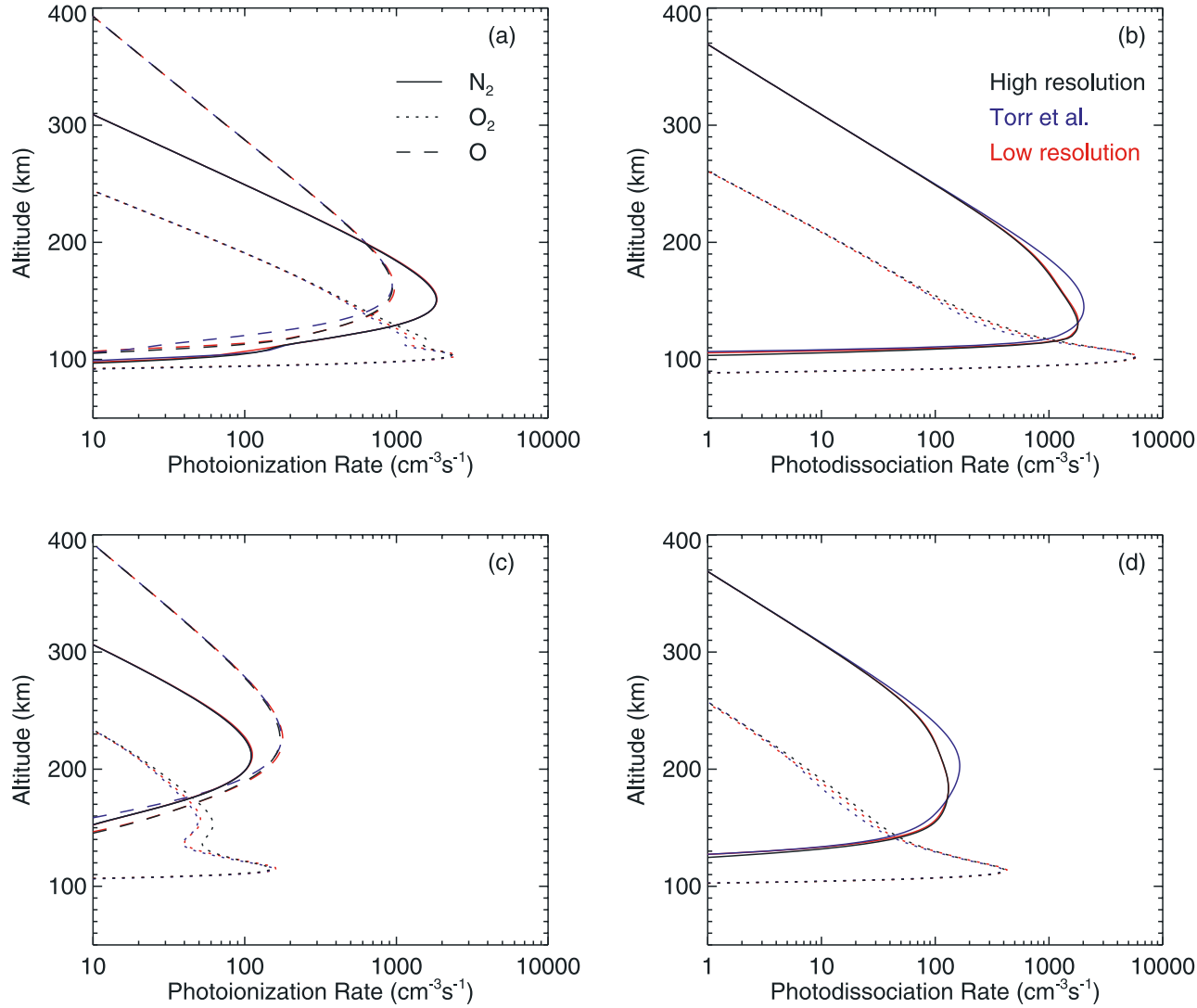

Figure 2. Photoionization and photodissociation rates in the EUV for major thermospheric species calculated using the EUVAC solar proxy model and MSIS-90 neutral atmosphere at $F_{10.7} = \langle F_{10.7} \rangle = 70$ for three spectral resolutions. Solid lines: N_2; dashed lines: O; dotted lines: O_2; black: high resolution (~0.1 nm); blue: *Torr et al.* [1979] method (5-nm bins and selected lines); red: new low-resolution scheme. (a) Photoionization rates for an overhead sun. (b) Photodissociation rates for an overhead sun. (c) Photoionization rates for a high solar zenith angle case (SZA = 85°). (d) Photodissociation rates for a high solar zenith angle case (SZA = 85°).

by this method for use by detailed process models, but these are the quantities important to general circulation model calculations and so are shown in this context.

[16] The solar actinic flux in each spectral interval at each level of the atmosphere is calculated by applying the Beer-Lambert law layer-by-layer through a model thermosphere:

$$I(\lambda, z) = I(\lambda, \infty) \exp[-\tau(\lambda, z)], \tag{4}$$

where the optical depth τ as a function of altitude z is

$$\tau(\lambda, z) = \Sigma_j \sigma_j(\lambda) N_j(z)/\mu \tag{5}$$

and N_j and σ_j are the column density and total absorption cross section for each species and μ is the cosine of the solar zenith angle. The process-specific rate for each species j and process k is then

$$R_{j,k}(z) = \Sigma_\lambda I(\lambda, z) \sigma_j(\lambda) \beta_{j,k}(\lambda), \tag{6}$$

where $\beta_{t,\varphi}$ is a branching ratio, e.g., for ionization, dissociative ionization, or dissociation.

[17] Comparison between photoionization and photodissociation calculations performed at various resolutions were made to assure the efficacy of the low-resolution scheme and to examine the accuracy of other methods used in previous work. The *Hinteregger et al.* [1981] SC21REFW high-resolution reference spectrum (individual lines with 0.1 nm resolution in the continua) was employed as the baseline. The *Torr et al.* [1979] 5-nm bins plus selected

lines, extended from 5.0 to 1.8 nm at with boundaries at the k-shell thresholds at 2.3 and 3.2 nm, was used as another basis for comparison. For both of these, the X-ray spectrum was further extended shortward with boundaries at 0.8, 0.4, 0.2, 0.1, and 0.05 nm. The results are displayed in Figure 2 for a low and a high solar zenith angle case. Very little difference is seen between the high-resolution and low-resolution methods. The only exception is at high solar zenith angles where slight differences are seen in the O_2 ionization rate. Other than this, the differences are generally less than 5%. The Torr et al. method also reproduces the high-resolution results reasonably well but has a significant discrepancy in the N_2 dissociation rate near the peak altitudes due to the structured cross sections in the 65–100 nm region and also underestimates O ionization rates. The low-resolution scheme is superior to the Torr et al. in this and in virtually all other respects, including increased computational efficiency due to fewer bins. Experiments at 1-nm resolution were also performed (not shown); this method results in excellent fidelity to the high-resolution calculations except in N_2 dissociation, where the curve lies between the Torr et al. and low-resolution results. In addition to adequate results for different solar zenith angles, it is also important that the method works well for different levels of solar activity. This was tested as well, but the results are equivalent to the low-activity results and so are not shown.

3. Photoelectron Effects

3.1. Modeling Calculations of Photoelectron Processes

[18] Ionization and dissociation of atmospheric gases by solar photons energizes the products of these processes, with the additional kinetic energy of the fragments equal to the energy of the photon minus the ionization potential or bond energy minus any residual excitation. In the case of ionizing processes, most of the energy is borne by the ejected electron, variously known as a secondary electron or photoelectron. These energetic electrons can also collide with neutral gases, ionizing them if they have sufficient energy and thereby creating more energetic electrons. They may travel significant distances before colliding, so the additional solar energy deposited through this process may be nonlocal. The additional ionization caused by photoelectron impact is small in the upper thermosphere (on the order of 10%) but increases with decreasing altitude, becoming the dominant process below ~120 km. Below ~100 km, photoelectron impact ionization becomes more than an order of magnitude greater than direct photoionization. Photoelectron impact is also an important source of dissociation, particularly of N_2 and so is crucial to the generation of odd-nitrogen. Excitation of atoms and molecules by photoelectrons further results in many of the well-known airglow emission features of the daytime thermosphere.

[19] Calculation of photoelectron fluxes and the resulting effects of their collisions may be accomplished using a modeling approach based on radiative transfer methods, with the cascade of electrons from high to low energies computed by considering the highest-energy electrons first and then solving for successively lower energies until near-thermal levels are reached. The two-stream method introduced by *Nagy and Banks* [1970] has been adopted by the GLOW model [*Solomon et al.*, 1988; *Solomon and Abreu*, 1989; *Bailey et al.*, 2002] and is applied here to calculation of ionization and dissociation rates due to photoelectron fluxes. However, this type of model is computationally prohibitive for a global time-dependent general circulation model, which necessitates some type of parameterized formulation. For the parameterization methodology described below, the model is employed using a neutral atmosphere specified by the MSIS-90 semi-empirical model [*Hedin*, 1991].

3.2. Parameterization of Photoelectron Ionization

[20] The basic concept behind the photoelectron parameterization method introduced here is that the ratio of photoelectron processes to direct photon processes depends on the energy of the photon. Since higher-energy photons have more excess energy following photoionization events, they have proportionally greater ability to create photoelectrons. Therefore we treat photoelectron processes separately in each spectral band, and then integrate over wavelength by summing the results for each band.

[21] The ratio of photoelectron impact ionization to direct photoionization, p_e/p_i, if known throughout the atmosphere for each species, can be used to multiply photoionization rates by the appropriate factor to obtain the total ionization rate. This can be accomplished by running a detailed photoelectron model such as GLOW for a variety of conditions, calculating p_e/p_i from the output, and obtaining some sort of parametric description of its variation. However, since this ratio is a complex function of altitude, solar zenith angle, solar activity, and composition, deriving a parameterization can be difficult. One simplifying technique [*Richards and Torr*, 1988] is to calculate the ratio as a function of individual-species optical depth at a key wavelength for each species and then apply the result to the photoionization rate as a function of altitude. This accounts for much of the altitude, solar zenith angle, and solar activity variation but is not very accurate due to its use of selected wavelengths (and hence cross sections) for the optical depth calculation.

[22] Our new method is based on a calculation of p_e/p_i as a function of optical depth in every bin of the low-resolution scheme. (It is equally applicable to any resolution.) To obtain these ratios, we repeatedly ran the GLOW model using the low-resolution spectrum but with only one bin active and the others all set to zero solar flux. This was done for a variety of conditions; in Figure 3 we show the results in four important bins for two solar zenith angle cases and two levels of solar activity. For each of these, p_e/p_i is a nearly constant function of optical depth, particularly at and below $\tau = 1$ (the peak of the ionization rate in each bin occurs at $\tau = 1$). Above this altitude, there is some variation, which can be difficult to quantify due to photoelectron transport effects which become important in the upper thermosphere. However, the total p_e/p_i is small at these heights. There is virtually no variation with solar activity, and the change with solar zenith angle is small. Therefore we elected to assign a single value, obtained at $\tau = 1$, for every bin and every species. These are tabulated in column 7 of Tables A2, A3, and A4. State-specific ratios are also given for O^+ production (Table A2) and bound/dissociated

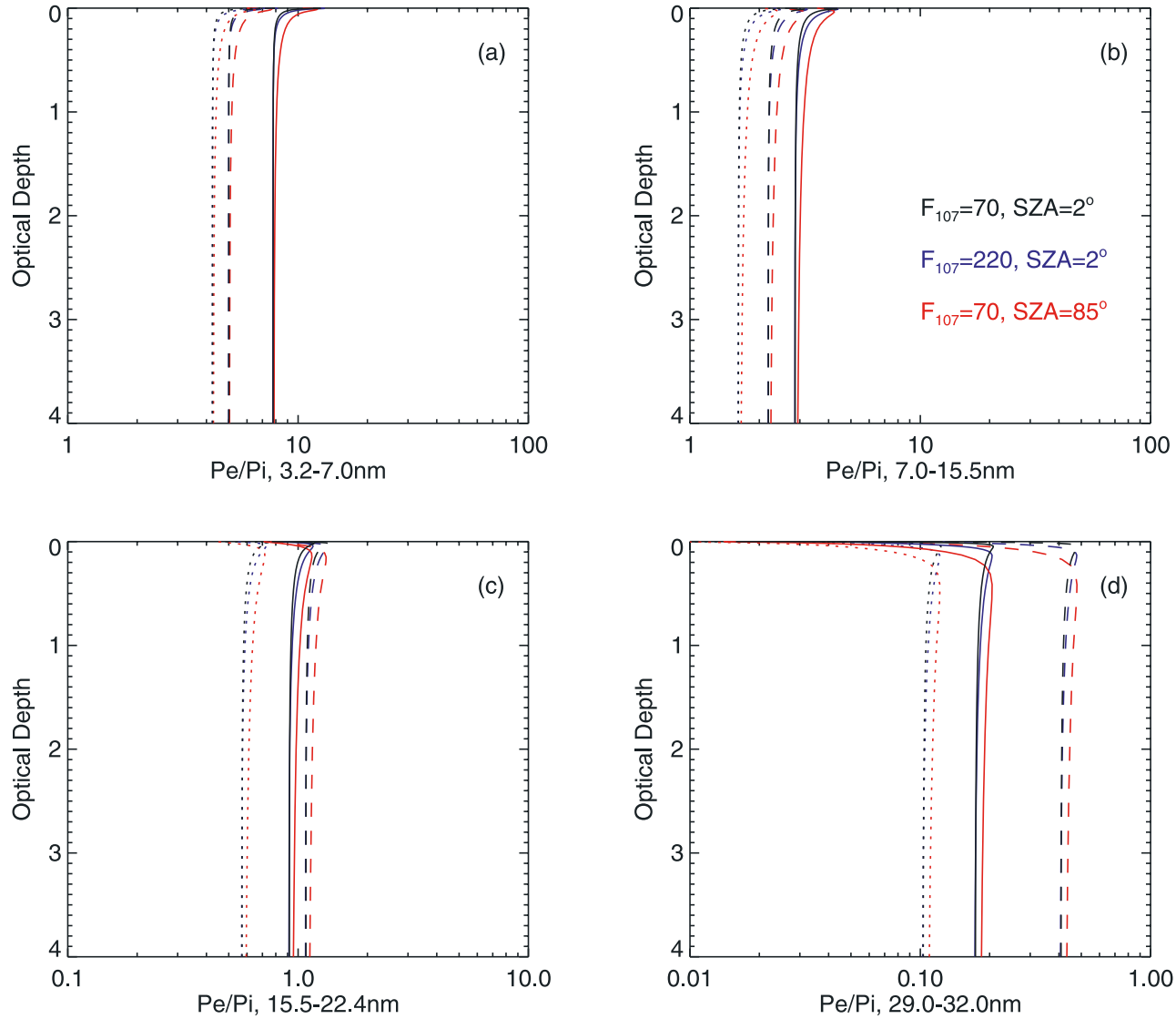

Figure 3. Photoelectron ionization enhancement factors p_e/p_i for four example spectral bins as a function of optical depth. Solid lines: N_2; dashed lines: O; dotted lines: O_2; black: $F_{10.7} = \langle F_{10.7} \rangle = 70$ and overhead sun; blue: $F_{10.7} = \langle F_{10.7} \rangle = 220$ and overhead sun; red: $F_{10.7} = \langle F_{10.7} \rangle = 70$ and SZA = 85°. (a) 3.2–7.0 nm. (b) 7.0–15.5 nm. (c) 15.5–22.4 nm. (d) 29.0–32.0 nm.

ratios for O_2 and N_2 (Table A3 and A4). Photoelectron impact ionization for each of these is then calculated by simply multiplying the ionization rate in each bin (equation (6)) by the appropriate ratio and summing over wavelength.

[23] Photoelectron enhancement factors p_e/p_i calculated using three different methods are plotted in Figure 4. These are the method described above, the method of *Richards and Torr* [1988], and a full calculation using the GLOW model. The EUVAC model at low and high activity was used as the solar input. Although the Richards and Torr method is clearly an improvement on use of a constant factor (as was employed by some models prior to its invention), it does not produce sufficient ionization at low altitude. Also, as pointed out by the authors, the amount of enhancement is sensitive to the assumed solar spectrum (for instance, the enhancement would be lower if calculated using the HFG model than using the EUVAC model) and also varies with solar activity, but this behavior is not captured by the parameterization. The new method does a good job of reproducing the GLOW model on which it is based and, since it calculates the enhancement in every spectral bin, varies appropriately with solar spectrum and solar activity. It also replicates detailed photoelectron calculations as the solar zenith angle changes. At high altitude, the parameterization starts to deviate from the full calculation because as photoelectron transport becomes important the nonlocal effects violate the assumptions on which the method is based. However, both the ionization rate and p_e/p_i become very small at these altitudes and have a negligible effect on thermospheric properties.

3.3. Parameterization of Photoelectron Dissociation

[24] Dissociation by photoelectrons is parameterized by a method analogous to the ionization enhancement described above. The GLOW model is run for each solar spectral bin, the ratio of photoelectron impact dissociation rate to pho-

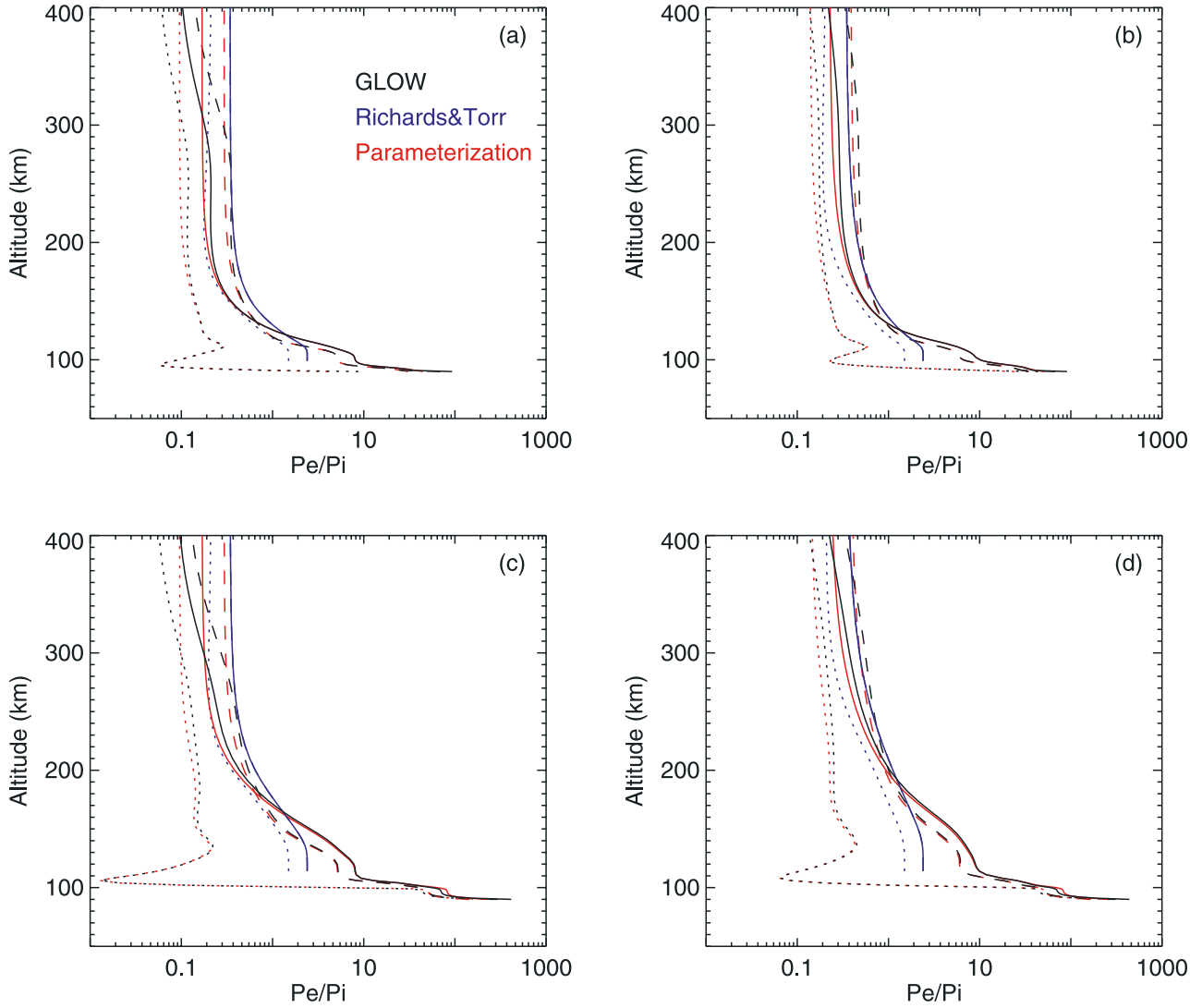

Figure 4. Comparison of photoelectron enhancement factors p_e/p_i calculated using three methods. Solid lines: N_2; dashed lines: O; dotted lines: O_2; black: full calculation using the GLOW model; blue: parameterization using the method of *Richards and Torr* [1988]; red: parameterization using the method described in the text. The Richards and Torr method is the same for N_2 and O. (a) $F_{10.7} = \langle F_{10.7} \rangle = 70$ and overhead Sun. (b) $F_{10.7} = \langle F_{10.7} \rangle = 220$ and overhead Sun. (c) $F_{10.7} = \langle F_{10.7} \rangle = 70$ and SZA = 85°. (d) $F_{10.7} = \langle F_{10.7} \rangle = 220$ and SZA = 85°.

toionization rate calculated as a function of optical depth for N_2 and O_2, and the value at $\tau = 1$ is selected as representative of that bin. The photoionization rate is used as the denominator because that is the process that generates the energetic electrons. These factors are tabulated in column 10 of Tables A3 and A4. They are employed in the same way as the ionization factors: The photoionization rate in each bin is calculated, multiplied by the dissociation factor, and then integrated over all bins to obtain the electron impact dissociation rate.

3.4. Comparison With Full Model Calculations

[25] The efficacy of this method is shown in Figure 5, where total ionization rates (photoionization plus photoelectron impact ionization) and total dissociation rates (photodissociation plus photoelectron impact dissociation) for each major species are compared to the full calculation using the GLOW model. Dissociative ionization is included in the ionization curves. For N_2, this represents all nonauroral dissociation; for O_2 the dissociation rate is dominated by photodissociation in the Schumann-Runge continuum by far-ultraviolet photons, and, in the mesosphere it is dominated by H Lyman-α at 121.6 nm. Effects from this spectral range are not shown here. Comparisons are shown for low and high solar zenith angle cases at low solar activity. High solar activity cases were also compared and have similar results but are not shown since the above discussion and previous examples explain why the new method is equally accurate for any solar spectrum. The only significant deviation of the parameterized method from the full calculation occurs at altitudes above ~300 km, where the nonlocal transport effects start to have an effect. Even

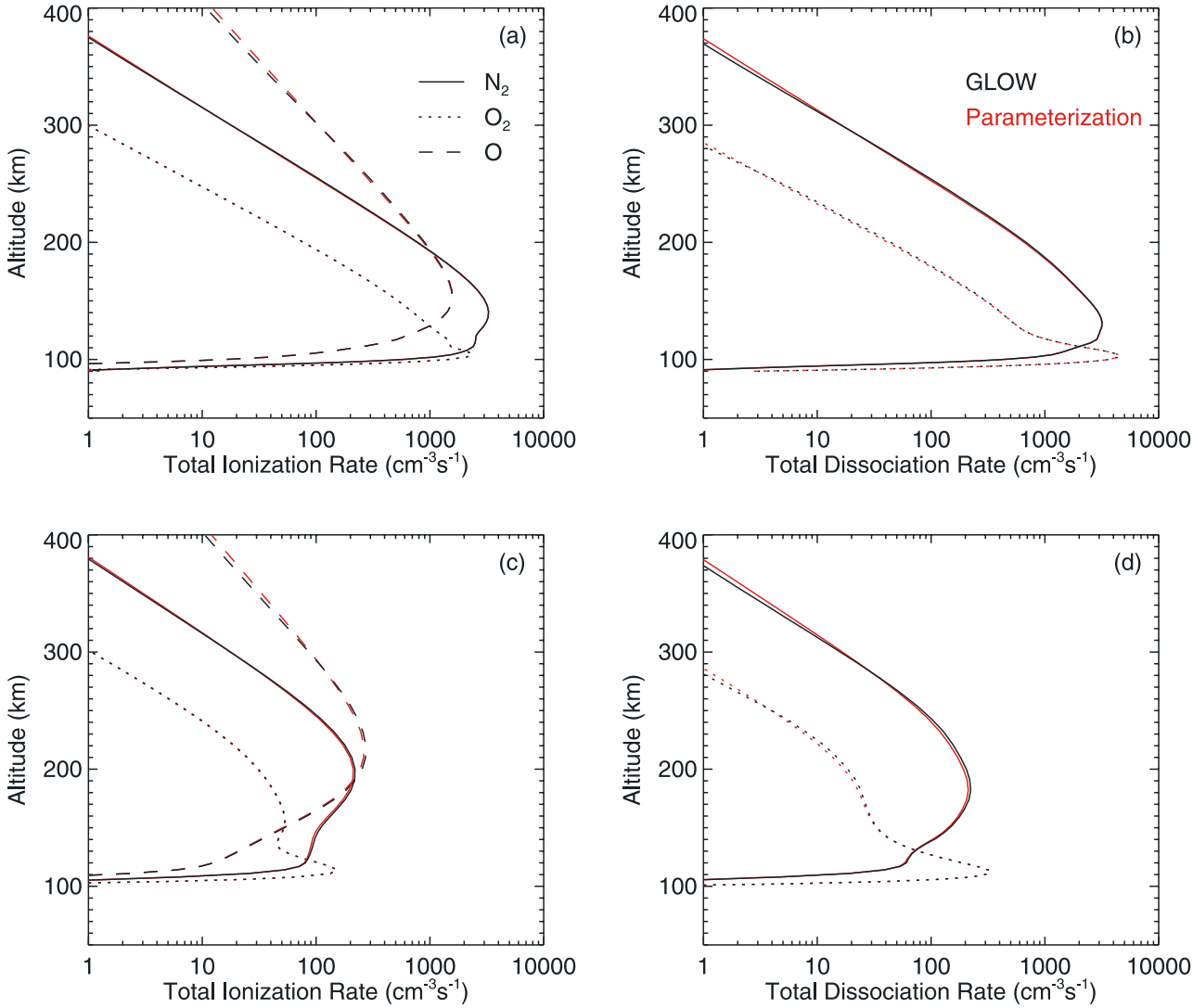

Figure 5. Total ionization and dissociation rates (direct photon plus photoelectron) in the EUV for major thermospheric species calculated using the EUVAC solar proxy model and MSIS-90 neutral atmosphere at $F_{10.7} = \langle F_{10.7} \rangle = 70$. Solid lines: N_2; dashed lines: O; dotted lines: O_2; black: full calculation using the GLOW model; red: parameterization using the method described in the text. (a) Total ionization rates for an overhead Sun. (b) Total dissociation rates for an overhead Sun. (c) Total ionization rates for a high solar zenith angle case (SZA = 85°). (d) Total dissociation rates for a high solar zenith angle case (SZA = 85°).

here, the agreement is within 10% and is within 5% throughout the lower altitudes.

4. Implementation of the Parameterization Method

4.1. Implementation in the NCAR TIE-GCM Using EUVAC

[26] The series of models developed at the National Center for Atmospheric Research (NCAR) by R. G. Roble and colleagues have used a variety of methods for specification of solar EUV ionization and photoelectron effects. The original thermosphere general circulation model (TGCM) [*Dickinson et al.*, 1981, 1984; *Roble et al.*, 1987] employed nine bands for solar EUV based on the HFG model and a constant factor for photoelectron ionization enhancement. The thermosphere-ionosphere general circulation model (TIGCM) [*Roble et al.*, 1988] used an extension of the HFG model in the *Torr et al.* [1979] bands [c.f., *Solomon and Roble*, 1992] and the *Richards and Torr* [1988] method for photoelectron ionization. The thermosphere-ionosphere-electrodynamics general circulation model (TIE-GCM) [*Richmond et al.*, 1992] and thermosphere-ionosphere-mesosphere-electrodynamics general circulation model (TIME-GCM) [*Roble and Ridley*, 1994; *Roble*, 1995] also used this method, but later versions included an option to use the EUVAC model and added an ad hoc soft X-ray term to account for additional photoelectron ionization at the shorter wavelengths.

[27] The new method described here is designed to replace the above for all wavelengths shortward of 105 nm, obviating the need for a separate X-ray module,

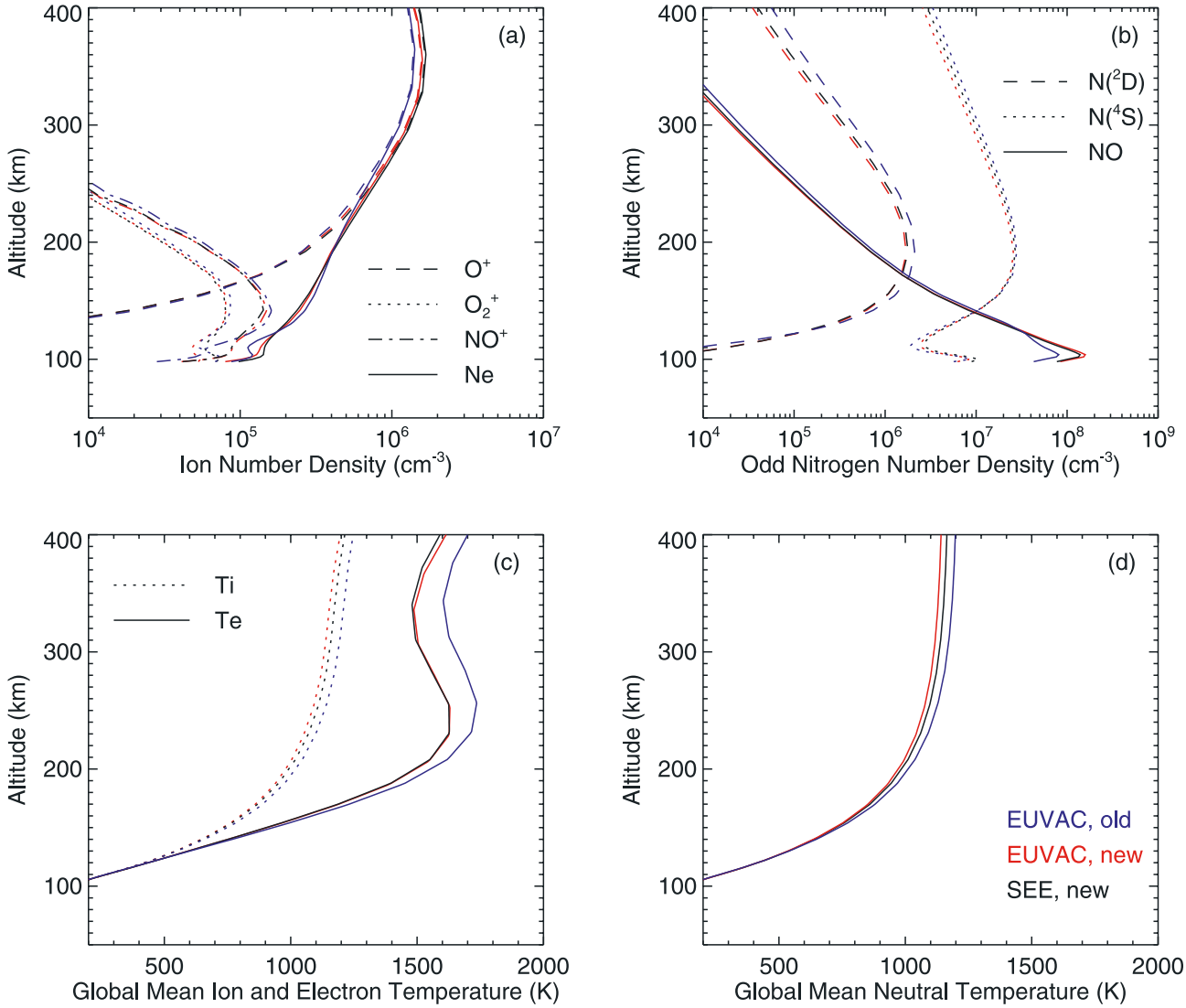

Figure 6. Application of the new bin structure and photoelectron parameterization method to the NCAR thermosphere-ionosphere-electrodynamics general circulation model (TIE-GCM). Blue: previous method using the EUVAC model as solar input; red: new method using the same solar input; black: new method using TIMED/SEE measurements as solar input. This example is obtained at UT = 0 on 30 March 2002 with $F_{10.7}$ = 188, $\langle F_{10.7} \rangle$ = 186. (a) Ion and electron number densities. Solid lines: electron density *Ne*; dashed lines: O^+; dotted lines: O_2^+, dot-dashed lines: NO^+. (b) Odd nitrogen number densities. Solid lines: NO; dashed lines: N(^2D); dotted lines: N(^4S). (c) Global mean ion and electron temperature. (d) Global mean neutral temperature. Figures 6a and 6b are at latitude 27.5°, longitude 165°, SZA = 28°; Figures 6c and 6d are global means.

and specifying photoelectron effects in a consistent as well as more accurate manner. It has been implemented in v. 1.8 of the TIE-GCM and has also been implemented in v. 3.0 of the whole atmosphere community climate model (WACCM) [e.g., *Sassi et al.*, 2004]. Comparison of results between the old and new methods, both using the EUVAC model as solar input, for key ionospheric and thermospheric parameters is shown in Figure 6. For the ionosphere, the main differences are seen in the *E* region, where the increased photoelectron ionization leads to higher electron density, in better agreement with observations and empirical models [c.f., *Solomon et al.*, 2001; *Solomon*, 2005]. Inclusion of fluxes shortward of 1.8 nm also adds a small amount of ionization to the lower *E* region. In the thermosphere, the most important effect is on odd-nitrogen in general and nitric oxide in particular, as the increased ionization and more complete treatment of dissociation causes a significant increase, particularly at low altitude. This is again in better agreement with recent observations [e.g., *Russell et al.*, 1993; *Barth et al.*, 1999; *Solomon et al.*, 1999; *Barth et al.*, 2003; *Marsh et al.*, 2004]. The other significant effect on the thermosphere is a small but significant lowering of temperatures throughout its extent, represented here by altitude plots of the global mean neutral, ion, and electron temperatures. This is due primarily to the increased nitric oxide density, through radiational cooling in its 5.3 μm band, which affects the entire thermospheric temperature profile despite its concentration at the lower levels. This will

Table A1. Solar Spectrum Parameters in the Low-Resolution Bin Structure

λ_{min}, nm	λ_{max}, nm	HFG f_{ref}, ph cm^{-2} s^{-1}	HFG c_1, ph cm^{-2} s^{-1}	HFG c_2, ph cm^{-2} s^{-1}	EUVAC f_{ref}, ph cm^{-2} s^{-1}	EUVAC A	SEE 3/30/04, ph cm^{-2}s^{-1}	SEE 2/8/02, ph cm^{-2}s^{-1}
0.05	0.4	5.010e+01	0.000e+00	2.948e+02	5.010e+01	6.240e-01	3.188e+04	7.847e+05
0.4	0.8	1.000e+04	0.000e+00	7.600e+03	1.000e+04	3.710e-01	3.643e+04	8.968e+05
0.8	1.8	2.000e+06	0.000e+00	4.600e+05	2.000e+06	2.000e-01	5.485e+06	1.046e+08
1.8	3.2	7.600e+06	7.470e+05	9.220e+05	2.850e+07	6.247e-02	6.317e+06	9.234e+07
3.2	7.0	1.659e+08	6.623e+07	4.293e+06	5.326e+08	1.343e-02	3.710e+08	1.475e+09
7.0	15.5	4.012e+08	1.662e+08	5.678e+06	1.270e+09	9.182e-03	1.023e+09	3.752e+09
15.5	22.4	2.078e+09	1.510e+08	6.273e+07	5.612e+09	1.433e-02	2.953e+09	1.144e+10
22.4	29.0	1.724e+09	3.310e+08	9.834e+07	4.342e+09	2.575e-02	4.927e+09	1.436e+10
29.0	32.0	6.793e+09	2.220e+09	4.286e+07	8.380e+09	7.059e-03	6.942e+09	1.234e+10
32.0	54.0	2.750e+09	5.469e+08	1.080e+08	2.861e+09	1.458e-02	6.486e+09	1.591e+10
54.0	65.0	5.035e+09	2.969e+09	1.590e+07	4.830e+09	5.857e-03	3.499e+09	6.213e+09
65.0	79.8	1.562e+09	6.938e+08	8.208e+06	1.459e+09	5.719e-03	1.869e+09	2.631e+09
65.0	79.8	1.264e+09	6.690e+08	5.445e+05	1.142e+09	3.680e-03	1.136e+09	1.540e+09
79.8	91.3	3.011e+09	3.011e+09	0.000e+00	2.364e+09	5.310e-03	3.494e+09	5.868e+09
79.8	91.3	4.661e+09	4.213e+09	0.000e+00	3.655e+09	5.261e-03	5.138e+09	8.562e+09
79.8	91.3	1.020e+09	1.020e+09	0.000e+00	8.448e+08	5.437e-03	1.306e+09	2.157e+09
91.3	97.5	5.441e+08	4.187e+08	0.000e+00	3.818e+08	4.915e-03	8.343e+08	1.373e+09
91.3	97.5	1.483e+09	1.307e+09	0.000e+00	1.028e+09	4.955e-03	1.866e+09	2.862e+09
91.3	97.5	8.642e+08	8.440e+08	0.000e+00	7.156e+08	4.422e-03	6.840e+08	1.111e+09
97.5	98.7	6.056e+09	3.671e+09	0.000e+00	4.482e+09	3.950e-03	4.139e+09	6.801e+09
98.7	102.7	5.569e+09	4.984e+09	0.000e+00	4.419e+09	5.021e-03	6.274e+09	1.019e+10
102.7	105.0	6.309e+09	5.796e+09	0.000e+00	4.235e+09	4.825e-03	4.389e+09	7.153e+09

necessitate readjustment of specific parameters relating to quenching rates but should actually bring the model into better accord with the recent laboratory evidence [*Hwang et al.*, 2003] and produce better solar cycle agreement with empirical models of exospheric temperature.

4.2. Implementation Using Selected Data From TIMED/SEE

[28] We have also used data from the SEE instrument on the NASA TIMED satellite [*Woods et al.*, 1998b, 2005] to drive the TIE-GCM. The procedure adopted is to perform an off-line sorting of the level 3, version 8 data into the low-resolution bins and then proceed as above. The level-3 data are daily averaged spectra at 1-nm resolution; with the exception of large flare intervals these data have sufficient temporal and spectral resolution for general circulation models. Data from 30 March 2002 at moderately high solar activity were used due to the proximity to equinox conditions. Although the spectral dependence of the measurements differs in detail from the EUVAC model (c.f., Figure 1) the net result is surprisingly similar, as the integrated energy flux between SEE and EUVAC are also similar. The model has also been run for other extended time periods using SEE data; this example is offered as indicative of new capabilities, since to our knowledge general circulation modeling of the thermosphere/ionosphere system has not previously been attempted using full-spectrum measurements of the solar EUV irradiance.

5. Discussion

[29] Any parameterization of this type is imperfect; the balance of efficiency and accuracy is the essence of the method. Although this scheme is accurate to within a few

Table A2. Cross Sections and Branching Factors for O

λ_{min}, nm	λ_{max}, nm	σ_{abs}, 10^{-18}cm^2	β ^4S	β ^2D	β ^2P	p_e/p_i total	p_e/p_i ^4S	p_e/p_i ^2D	p_e/p_i ^2P
0.05	0.4	0.0023	0.390	0.378	0.224	217.12	81.240	88.526	47.358
0.4	0.8	0.0170	0.390	0.378	0.224	50.593	18.896	20.691	11.007
0.8	1.8	0.1125	0.390	0.378	0.224	23.562	9.425	9.365	4.772
1.8	3.2	0.1050	0.390	0.378	0.224	71.378	28.622	28.199	14.556
3.2	7.0	0.3247	0.393	0.374	0.226	4.995	2.019	1.962	1.014
7.0	15.5	1.3190	0.389	0.377	0.227	2.192	0.902	0.853	0.436
15.5	22.4	3.7832	0.367	0.392	0.233	1.092	0.470	0.418	0.203
22.4	29.0	6.0239	0.350	0.402	0.241	0.694	0.325	0.253	0.116
29.0	32.0	7.7205	0.346	0.403	0.246	0.418	0.209	0.148	0.061
32.0	54.0	10.7175	0.317	0.424	0.260	0.127	0.084	0.034	0.009
54.0	65.0	13.1253	0.298	0.451	0.252	0.000	0.000	0.000	0.000
65.0	79.8	8.5159	0.655	0.337	0.009	0.000	0.000	0.000	0.000
65.0	79.8	4.7889	0.930	0.070	0.000	0.000	0.000	0.000	0.000
79.8	91.3	3.0031	1.000	0.000	0.000	0.000	0.000	0.000	0.000
79.8	91.3	4.1048	1.000	0.000	0.000	0.000	0.000	0.000	0.000
79.8	91.3	3.7947	1.000	0.000	0.000	0.000	0.000	0.000	0.000
91.3	97.5	0.0000	0.000	0.000	0.000	0.000	0.000	0.000	0.000
91.3	97.5	0.0000	0.000	0.000	0.000	0.000	0.000	0.000	0.000
91.3	97.5	0.0000	0.000	0.000	0.000	0.000	0.000	0.000	0.000
97.5	98.7	0.0000	0.000	0.000	0.000	0.000	0.000	0.000	0.000
98.7	102.7	0.0000	0.000	0.000	0.000	0.000	0.000	0.000	0.000
102.7	105.0	0.0000	0.000	0.000	0.000	0.000	0.000	0.000	0.000

Table A3. Cross Sections, and Branching Ratios, and Photoelectron Factors for O_2

λ_{min}, nm	λ_{max}, nm	σ_{abs}, $10^{-18}cm^2$	β O_2^+	β D. I.	β Dissoc.	p_e/p_i total	p_e/p_i O_2^+	p_e/p_i D. I.	p_e/p_i Dissoc.
0.05	0.4	0.0045	0.000	1.000	0.000	210.83	134.69	76.136	87.864
0.4	0.8	0.0340	0.000	1.000	0.000	50.156	32.212	17.944	20.318
0.8	1.8	0.2251	0.000	1.000	0.000	20.290	13.309	6.981	17.821
1.8	3.2	0.2101	0.000	1.000	0.000	59.953	39.615	20.338	56.969
3.2	7.0	0.6460	0.108	0.892	0.000	4.271	2.834	1.437	4.113
7.0	15.5	2.6319	0.347	0.653	0.000	1.613	1.092	0.521	2.041
15.5	22.4	7.6283	0.553	0.447	0.000	0.579	0.416	0.163	1.271
22.4	29.0	13.2125	0.624	0.376	0.000	0.242	0.189	0.052	0.996
29.0	32.0	16.8233	0.649	0.351	0.000	0.105	0.090	0.014	0.762
32.0	54.0	20.3066	0.759	0.240	0.000	0.024	0.023	0.001	0.653
54.0	65.0	27.0314	0.874	0.108	0.017	0.000	0.000	0.000	0.011
65.0	79.8	23.5669	0.672	0.001	0.327	0.000	0.000	0.000	0.000
65.0	79.8	24.9102	0.477	0.000	0.524	0.000	0.000	0.000	0.000
79.8	91.3	10.4980	0.549	0.000	0.451	0.000	0.000	0.000	0.000
79.8	91.3	10.9075	0.574	0.000	0.426	0.000	0.000	0.000	0.000
79.8	91.3	13.3122	0.534	0.000	0.466	0.000	0.000	0.000	0.000
91.3	97.5	13.3950	0.756	0.000	0.244	0.000	0.000	0.000	0.000
91.3	97.5	14.4042	0.786	0.000	0.214	0.000	0.000	0.000	0.000
91.3	97.5	32.5038	0.620	0.000	0.380	0.000	0.000	0.000	0.000
97.5	98.7	18.7145	0.830	0.000	0.170	0.000	0.000	0.000	0.000
98.7	102.7	1.6320	0.613	0.000	0.387	0.000	0.000	0.000	0.000
102.7	105.0	1.1500	0.000	0.000	1.000	0.000	0.000	0.000	0.000

percent for the quantities that are most important, the total ionization and dissociation in the peak regions, it degrades to ~10% accuracy at very high altitude due to the neglect of photoelectron transport. This could be improved by the use of altitude-dependent photoelectron enhancement factors in each bin. There is also a small discrepancy in O_2 ionization rates at high solar zenith angle which could be improved by the addition of a few more bins. However, the new scheme is both more accurate and more efficient than its predecessor, which has been used with reasonable results for some time. There is little point in trying to increase its accuracy at the expense of efficiency while large uncertainties still exist in the solar spectrum and its variation, not to mention atmospheric cross sections, which are better known than the former, but in the EUV range have uncertainties far greater than those introduced by our parameterization.

[30] The most significant problem for solar irradiances is still in the soft X-ray region, and becomes worse with decreasing wavelength. This is partly due to the dearth of relevant measurements, especially in the ~1 to ~3 nm region, partly to instrument calibration difficulties, partly to the broadband nature of many of the available measurements, and partly to the challenges involved with modeling very highly ionized emission where transition parameters are not entirely well established. The problem is exacerbated by solar flare effects, not just large flares where the soft X-ray spectrum is highly variable and not well-quantified, but also by the many small flares that contribute in the aggregate to atmospheric ionization. Until better spectrally resolved measurements are available, it is difficult to justify the addition of spectral resolution to the model at the shortest wavelengths. However, this scheme is well-suited to the incorporation of available high-time-cadence measurements below 0.8 nm by the GOES X-ray sensors. From a solar modeling point of view, a flare index based on such measurements, even if imperfect, would be a logical addi-

Table A4. Cross Sections, and Branching Ratios, and Photoelectron Factors for N_2

λ_{min}, nm	λ_{max}, nm	σ_{abs}, $10^{-18}cm^2$	β N_2^+	β D. I.	β Dissoc.	p_e/p_i total	p_e/p_i N_2^+	p_e/p_i D. I.	p_e/p_i Dissoc.
0.05	0.4	0.0025	0.040	0.960	0.000	342.66	263.99	78.674	245.00
0.4	0.8	0.0201	0.040	0.960	0.000	80.880	62.570	18.310	52.052
0.8	1.8	0.1409	0.040	0.960	0.000	32.162	25.213	6.948	25.255
1.8	3.2	1.1370	0.040	0.960	0.000	10.834	8.540	2.295	9.049
3.2	7.0	0.3459	0.717	0.282	0.000	7.789	6.142	1.647	6.532
7.0	15.5	1.5273	0.751	0.249	0.000	2.859	2.288	0.571	2.909
15.5	22.4	5.0859	0.747	0.253	0.000	0.933	0.786	0.146	1.371
22.4	29.0	9.9375	0.754	0.246	0.000	0.361	0.324	0.037	0.764
29.0	32.0	11.7383	0.908	0.093	0.000	0.178	0.169	0.008	0.515
32.0	54.0	19.6514	0.996	0.005	0.000	0.031	0.031	0.000	0.157
54.0	65.0	23.0931	1.000	0.000	0.000	0.000	0.000	0.000	0.000
65.0	79.8	23.0346	0.679	0.000	0.320	0.000	0.000	0.000	0.000
65.0	79.8	54.5252	0.429	0.000	0.571	0.000	0.000	0.000	0.000
79.8	91.3	2.1434	0.000	0.000	1.000	0.000	0.000	0.000	0.000
79.8	91.3	13.1062	0.000	0.000	1.000	0.000	0.000	0.000	0.000
79.8	91.3	71.6931	0.000	0.000	1.000	0.000	0.000	0.000	0.000
91.3	97.5	2.1775	0.000	0.000	1.000	0.000	0.000	0.000	0.000
91.3	97.5	14.4390	0.000	0.000	1.000	0.000	0.000	0.000	0.000
91.3	97.5	115.257	0.000	0.000	1.000	0.000	0.000	0.000	0.000
97.5	98.7	2.5465	0.000	0.000	1.000	0.000	0.000	0.000	0.000
98.7	102.7	0.0000	0.000	0.000	0.000	0.000	0.000	0.000	0.000
102.7	105.0	0.0000	0.000	0.000	0.000	0.000	0.000	0.000	0.000

tion to the terrestrial modeling suite, particularly due to current interest in mesospheric and *D* region effects. The examples shown here are implemented using empirical model atmospheres and in the TIE-GCM since those altitude ranges are appropriate for the EUV development, but one goal of this research is to obtain a unified methodology for all of the NCAR upper atmosphere modeling suite, including the TIME-GCM and WACCM, and to make it available to other upper-atmosphere models. The method is adaptable with respect to the solar input so that as measurements and models of solar spectral irradiance in the EUV and X-ray regions become available they may be incorporated. With new spectrally resolved rocket-based and satellite-based observations planned in the soft X-ray range, we anticipate continued improvement in our ability to quantitatively predict the thermosphere and ionosphere density and temperature response to solar forcing using numerical models.

Appendix A

[31] The derived parameters that form the basis of the parameterization scheme described here are specified in the following tables. Solar parameters for the extended HFG and EUVAC models, and for low-activity and high-activity TIMED/SEE (version 8) spectra on 30 March 2004 and 8 February 2002, are given in Table A1. Note that from 1.8–5.0 nm the factors in the EUVAC column are based on the HFG model but scaled upward by a factor of 3. See section 2.1 for a discussion of the 0.5–1.8 nm estimates. The 0.8–1.8 nm bin in particular has a high uncertainty and the values should be considered to be very preliminary. Cross sections, branching ratios, photoelectron ionization factors, and photoelectron dissociation factors, are given in Tables A2, A3, and A4 for O, O_2, and N_2, respectively.

[32] **Acknowledgments.** The authors thank Thomas N. Woods, Francis G. Eparvier, and Scott M. Bailey for assistance with TIMED/SEE data, Raymond G. Roble, Arthur D. Richmond, Wenbin Wang, and Benjamin Foster for assistance with the TIE-GCM, and Astrid Maute for comments on the manuscript. This research was supported by NASA grants NAG5-5335 and NAG5-11410 to the National Center for Atmospheric Research. NCAR is supported by the National Science Foundation.

[33] Shadia Rifai Habbal thanks Harry P. Warren and another referee for their assistance in evaluating this paper.

References

Acton, L. W., D. C. Weston, and M. E. Bruner (1999), Deriving solar X-ray irradiance from Yohkoh observations, *J. Geophys. Res.*, *104*, 14,827.

Bailey, S. M., C. A. Barth, M. J. Erickson, R. A. Kohnert, A. W. Merkel, E. M. Rodgers, S. C. Solomon, S. D. Straight, J. E. Vian, and T. N. Woods (1996), Science instrumentation for the Student Nitric Oxide Explorer, *Proc. SPIE Int. Soc. Opt. Eng.*, *2830*, 264.

Bailey, S. M., T. N. Woods, L. R. Canfield, R. Korde, C. A. Barth, S. C. Solomon, and G. J. Rottman (1999a), Sounding rocket measurements of the solar soft X-ray irradiance, *Sol. Phys.*, *186*, 243.

Bailey, S. M., T. N. Woods, C. A. Barth, and S. C. Solomon (1999b), Measurements of the solar soft X-ray irradiance from the Student Nitric Oxide Explorer, *Geophys. Res. Lett.*, *26*, 1255.

Bailey, S. M., T. N. Woods, C. A. Barth, S. C. Solomon, L. R. Canfield, and R. Korde (2000), Measurements of the solar soft X-ray irradiance from the Student Nitric Oxide Explorer: First analysis and underflight calibrations, *J. Geophys. Res.*, *105*, 27,179.

Bailey, S. M., T. N. Woods, C. A. Barth, S. C. Solomon, L. R. Canfield, and R. Korde (2001), Correction to "Measurements of the solar soft X-ray irradiance from the Student Nitric Oxide Explorer: First analysis and underflight calibrations," *J. Geophys. Res.*, *106*, 15,791.

Bailey, S. M., C. A. Barth, and S. C. Solomon (2002), A model of nitric oxide in the thermosphere, *J. Geophys. Res.*, *107*(A8), 1205, doi:10.1029/2001JA000258.

Barth, C. A., S. M. Bailey, and S. C. Solomon (1999), Solar-terrestrial coupling: Solar soft X-rays and thermospheric nitric oxide, *Geophys. Res. Lett.*, *26*, 1251.

Barth, C. A., K. D. Mankoff, S. M. Bailey, and S. C. Solomon (2003), Global observations of nitric oxide in the thermosphere, *J. Geophys. Res.*, *108*(A1), 1027, doi:10.1029/2002JA009458.

Buonsanto, M. J., S. C. Solomon, and W. K. Tobiska (1992), Comparison of measured and modeled solar EUV flux and its effect on the E-F1 region of the ionosphere, *J. Geophys. Res.*, *97*, 10,513.

Buonsanto, M. J., P. G. Richards, W. K. Tobiska, S. C. Solomon, Y.-K. Tung, and J. A. Fennelly (1995), Ionospheric electron densities calculated using different EUV flux models and cross sections: Comparison with radar data, *J. Geophys. Res.*, *100*, 14,569.

Conway, R. R. (1988), Photoabsorption and photoionization cross section of O, O_2, and N_2 for photoelectron production calculations: A compilation of recent laboratory measurements, *NRL Mem. Rep. 6155*, Naval Res. Lab., Washington, D. C.

DeJager, C. (1964), Solar X-radiation, in *Astronomical Observations From Space Vehicles*, edited by J.-L. Steinberg, p. 45, Taffin-Lefort, Liège, Belgium.

Dickinson, R. E., E. C. Ridley, and R. G. Roble (1981), A three-dimensional general circulation model of the thermosphere, *J. Geophys. Res.*, *86*, 1499.

Dickinson, R. E., E. C. Ridley, and R. G. Roble (1984), Thermospheric general circulation with coupled dynamics and composition, *J. Atmos. Sci.*, *41*, 205.

Donnelly, R. F. (1976), Empirical models of solar flare X-ray and EUV emissions for use in studying the *E* and *F* region effects, *J. Geophys. Res.*, *81*, 4745.

Hall, L. A., and H. E. Hinteregger (1970), Solar radiation in the extreme ultraviolet and its variation with solar rotation, *J. Geophys. Res.*, *75*, 6959.

Hall, L. W., J. E. Higgins, C. W. Chagnon, and H. E. Hinteregger (1969), Solar cycle variation of extreme ultraviolet radiation, *J. Geophys. Res.*, *74*, 4181.

Heroux, L., and J. E. Higgins (1977), Summary of full-disk solar fluxes between 250 and 1940 Å, *J. Geophys. Res.*, *82*, 3307.

Hedin, A. E. (1991), Extension of the MSIS thermosphere model into the middle and lower atmosphere, *J. Geophys. Res.*, *96*, 1159.

Henke, B. L., E. M. Gullikson, and J. C. Davis (1993), X-ray interactions: Photoabsorption, scattering, transmission, and reflection at E = 50–30,000 eV, Z = 1–92, *At. Data Nucl. Data Tables*, *54*, 181.

Hinteregger, H. E., K. Fukui, and B. R. Gilson (1981), Observational, reference, and model data on solar EUV, from measurements on AE–E, *Geophys. Res. Lett.*, *8*, 1147.

Horan, D. M., and R. W. Kreplin (1981), Simultaneous measurements of EUV and soft X-ray solar flare emission, *Solar Phys.*, *74*, 265.

Hwang, E. S., K. J. Castle, and J. A. Dodd (2003), Vibrational relaxation of NO(v = 1) by oxygen atoms between 295 and 825 K, *J. Geophys. Res.*, *108*(A3), 1109, doi:10.1029/2002JA009688.

Feng, W., H. S. Ogawa, and D. L. Judge (1989), The absolute solar soft X-ray flux in the 20–100 Å region, *J. Geophys. Res.*, *94*, 9125.

Fennelly, J. A., and D. G. Torr (1992), Photoionization and photoabsorption cross sections of O, N_2, O_2, and N for aeronomic calculations, *At. Data Nucl. Data Tables*, *51*, 321.

Judge, D. L., et al. (1998), First solar EUV irradiances obtained from SOHO by the CELIAS/SEM, *Solar Phys.*, *177*, 161.

Kirby, K., E. R. Constantinides, S. Babeu, M. Oppenheimer, and G. A. Victor (1979), Photoionization and photoabsorption cross sections of thermospheric species: He, O, N_2, and O_2, *At. Data Nucl. Data Tables*, *23*, 63–81.

Kreplin, R. W., K. P. Dere, D. M. Horan, and J. F. Meekins (1977), The solar spectrum below 10 Å, in *The Solar Output and its Variation*, edited by O. R. White, p. 287, Colo. Assoc. Univ. Press, Boulder, Colo.

Manson, J. E. (1977), The solar spectrum between 10 and 300 Å, in *The Solar Output and its Variation*, edited by O. R. White, p. 261, Colo. Assoc. Univ. Press, Boulder, Colo.

Marsh, D. R., S. C. Solomon, and A. E. Reynolds (2004), Empirical model of nitric oxide in the lower thermosphere, *J. Geophys. Res.*, *109*, A07301, doi:10.1029/2003JA010199.

Nagy, A. F., and P. M. Banks (1970), Photoelectron fluxes in the ionosphere, *J. Geophys. Res.*, *75*, 6260.

Ogawa, H. S., L. R. Canfield, D. McMullin, and D. L. Judge (1990), Sounding rocket measurement of the absolute solar EUV flux utilizing a silicon photodiode, *J. Geophys. Res.*, *95*, 4291.

Reeves, E. M., and W. H. Parkinson (1970), An atlas of extreme-ultraviolet spectroheliograms from OSO-IV, *Astrophys. J. Suppl.*, *181*, 1.

Richards, P. G., and D. G. Torr (1984), An investigation of the consistency of the ionospheric measurements of the photoelectron flux and solar EUV flux, *J. Geophys. Res.*, *89*, 5625.

Richards, P. G., and D. G. Torr (1988), Ratios of photoelectron to EUV ionization rates for aeronomic studies, *J. Geophys. Res.*, *93*, 4060.

Richards, P. G., J. A. Fennelly, and D. G. Torr (1994), EUVAC: A solar EUV flux model for aeronomic calculations, *J. Geophys. Res.*, *99*, 8981.

Richmond, A. D., E. C. Ridley, and R. G. Roble (1992), A thermosphere/ionosphere general circulation model with coupled electrodynamics, *Geophys. Res. Lett.*, *19*, 601.

Roble, R. G. (1995), Energetics of the mesosphere and thermosphere, in *The Upper Mesosphere and Lower Thermosphere: A Review of Experiment and Theory*, *Geophys. Monogr. Ser.*, vol. 87, edited by R. M. Johnson and T. L. Killeen, p. 1, AGU, Washington, D. C.

Roble, R. G., and E. C. Ridley (1994), Thermosphere-ionosphere-mesosphere-electrodynamics general circulation model (TIME-GCM): Equinox solar min simulations, 30–500 km, *Geophys. Res. Lett.*, *21*, 417.

Roble, R. G., E. C. Ridley, and R. E. Dickinson (1987), On the global mean structure of the thermosphere, *J. Geophys. Res.*, *92*, 8745.

Roble, R. G., E. C. Ridley, A. D. Richmond, and R. E. Dickinson (1988), A coupled thermosphere/ionosphere general circulation model, *Geophys. Res. Lett.*, *15*, 1325.

Russell, J. M., III, et al. (1993), The Halogen Occultation Experiment, *J. Geophys. Res.*, *98*, 10,777.

Sassi, F., D. Kinnison, B. A. Boville, R. R. Garcia, and R. Roble (2004), The effect of ENSO on the dynamical, thermal and chemical structure of the middle atmosphere, *J. Geophys. Res.*, *109*, D17108, doi:10.1029/2003JD004434.

Schmidtke, G., K. Rawer, H. Botzek, D. Norbert, and K. Holzer (1977), Solar EUV photon fluxes measured aboard AEROS A, *J. Geophys. Res.*, *82*, 2423.

Schmidtke, G., T. N. Woods, J. Worden, G. J. Rottman, H. Doll, C. Wita, and S. C. Solomon (1992), Solar EUV irradiance from the San Marco ASSI: A reference spectrum, *Geophys. Res. Lett.*, *19*, 2175.

Smith, E. V. P., and D. M. Gottlieb (1974), Solar flux and its variations, *Space Sci. Rev.*, *16*, 771.

Solomon, S. C. (1991), Optical aeronomy, *Rev. Geophys.*, *29*, 1089.

Solomon, S. C. (2005), Numerical models of the E-region ionosphere, *Adv. Space Res.*, in press.

Solomon, S. C., and V. J. Abreu (1989), The 630 nm dayglow, *J. Geophys. Res.*, *94*, 6817.

Solomon, S. C., and R. G. Roble (1992), Temperature variation in the thermosphere: Simulations using the NCAR Thermosphere/Ionosphere General Circulation Model, in *SOLERS22: Proceedings of the Workshop on the Solar Electromagnetic Radiation Study for Solar Cycle 22*, edited by R. F. Donnelly, p. 399, NOAA, Boulder, Colo.

Solomon, S. C., P. B. Hays, and V. J. Abreu (1988), The auroral 6300 Å emission: Observations and modeling, *J. Geophys. Res.*, *93*, 9867.

Solomon, S. C., et al. (1996), The Student Nitric Oxide Explorer, *Proc. SPIE Int. Soc. Opt. Eng.*, *2810*, 121.

Solomon, S. C., C. A. Barth, and S. M. Bailey (1999), Auroral production of nitric oxide measured by the SNOE Satellite, *Geophys. Res. Lett.*, *26*, 1259.

Solomon, S. C., S. M. Bailey, and T. N. Woods (2001), Effect of solar soft X-rays on the lower ionosphere, *Geophys. Res. Lett.*, *28*, 2149.

Strickland, D. J., J. L. Lean, R. R. Meier, A. B. Christensen, L. J. Paxton, D. Morrison, J. D. Craven, R. L. Walterscheid, D. L. Judge, and D. R. McMullin (2004), Solar EUV irradiance variability derived from terrestrial far ultraviolet dayglow observations, *Geophys. Res. Lett.*, *31*, L03801, doi:10.1029/2003GL018415.

Tobiska, W. K., T. N. Woods, F. Eparvier, R. Viereck, L. Floyd, D. Bouwer, G. Rottman, O. R. White, and R. F. Donnelly (2000), The SOLAR2000 empirical solar irradiance model and forecast tool, *J. Atmos. Solar Terr. Phys.*, *62*, 1233–1250.

Torr, M. R., D. G. Torr, R. A. Ong, and H. E. Hinteregger (1979), Ionization frequencies for major thermospheric constituents as a function of solar cycle 21, *Geophys. Res. Lett.*, *6*, 771.

Wagner, W. J. (1988), Observations of 1–8 Å solar X-ray variability during solar cycle 21, *Adv. Space Res.*, *8*, 67.

Warren, H. P., J. T. Mariska, and J. Lean (2001), A new model of solar EUV irradiance variability, 1, model formulation, *J. Geophys. Res.*, *106*, 15,745.

Winningham, J. D., D. T. Decker, J. U. Kozyra, J. R. Jasperse, and A. F. Nagy (1989), Energetic (>60 eV) atmospheric photoelectrons, *J. Geophys. Res.*, *94*, 15,335.

Woods, T. N., and G. J. Rottman (2002), Solar ultraviolet variability over time periods of aeronomic interest, in *Comparative Aeronomy in the Solar System*, *Geophys. Monogr. Ser.*, vol. 130, edited by M. Mendillo, A. F. Nagy, and J. H. Waite, AGU, Washington, D. C.

Woods, T. N., G. J. Rottman, S. M. Bailey, S. C. Solomon, and J. R. Worden (1998a), Solar extreme ultraviolet irradiance measured during solar cycle 22, *Solar Phys.*, *177*, 133.

Woods, T. N., S. M. Bailey, F. Eparvier, G. Lawrence, J. Lean, W. McClintock, R. Roble, G. Rottman, S. C. Solomon, W. K. Tobiska, G. Ucker, and O. R. White (1998b), TIMED Solar EUV experiment, *Proc. SPIE*, *3442*, 180.

Woods, T. N., et al. (2004), Solar extreme ultraviolet and X-ray irradiance variations, in *Solar Variability and Its Effect on Climate*, *Geophys. Monogr. Ser.*, vol. 141, edited by J. M. Pap et al., p. 127, AGU, Washington, D. C.

Woods, T. N., F. G. Eparvier, S. M. Bailey, P. C. Chamberlain, J. Lean, G. J. Rottman, S. C. Solomon, W. K. Tobiska, and D. Woodraska (2005), The Solar EUV Experiment (SEE): Mission overview and first results, *J. Geophys. Res.*, *110*, A01312, doi:10.1029/2004JA010765.

L. Qian and S. C. Solomon, High Altitude Observatory,National Center for Atmospheric Research, 1850 Table Mesa Drive, Boulder, CO 80307-3000, USA. (stans@ucar.edu)